Enhanced Hole Expansion Predictions for Laser-Polished DP1000 Steel Using Multiscale Simulation

Journal of Physics: Conference Series **3104** (2025) 012026 doi:10.1088/1742-6596/3104/1/012026

Enhanced Hole Expansion Predictions for Laser-Polished DP1000 Steel Using Multiscale Simulation

Dongsong Li[1*], Berk Tekkaya[1] and Sebastian Münstermann[1]

[1] Institute of Metal Forming, RWTH Aachen University, Aachen, Germany

[*]E-mail: dongsong.li@ibf.rwth-aachen.de

Abstract. A multiscale FE simulation has been conducted for DP1000 sheet material with a thickness of 1.5 mm, which exhibits enhanced edge roughness due to laser-polishing. A smoother geometry and a new martensitic structure at the edge were observed during the laser-polishing process for the hole expansion sample. The effects of this new edge geometry are considered in the macroscopic simulation. The material characterization of the martensitic microstructure is performed based on the findings from heat treatment experiments. The coupled modified Bai-Wierzbicki (MBW) damage model is employed to predict damage behavior in the macroscopic simulation of the hole expansion test. In the microscopic simulation, the same material characterization resulting from heat treatment was applied, while local roughness was represented using actual measured roughness data. The macroscopic simulation's damage criterion has been optimized by utilizing surface parameters. Bridging the roughness information from the microscopic simulation to the macroscopic simulation demonstrates that simulation results better agree with experimental outcomes.

1. Introduction

Dual-phase (DP) steels are widely utilized in industries such as automotive due to their excellent mechanical properties, including high strength, ductility, strain hardening, and crashworthiness. The microstructure consists of a soft ferritic matrix with hard martensite at grain boundaries, resulting in a low yield-to-tensile ratio and good formability [1, 2]. However, they exhibit sensitivity to edge cracking, especially when shear cutting introduces significant edge damage and roughness. The hole expansion test is a typical material testing procedure to evaluate the edge crack sensitivity [3]. To enhance local formability and reduce edge crack sensitivity, controlling the microstructural features of DP steels has been explored. Reducing the strength contrast between phases can improve the hole expansion ratio (HER), leading to finer grain sizes and more uniform microstructures [4]. Laser-polishing has emerged as an effective technique to improve edge quality at the macroscopic level. Using a high-energy laser beam to melt and smooth surface imperfections through surface tension effects in the liquid state, laser polishing reshapes and reinforces edge geometry, significantly increasing fatigue strength and local formability compared to conventional methods [5]. Numerical approaches have gained attention for predicting local formability using a coupled damage model, e.g., the modified Bai-Wierzbicki model (MBW) [6, 7]. The MBW model addresses these materials' damage evolution by describing the stress-state dependency of ductile damage evolution from initiation to fracture, evaluating the equivalent plastic strain to determine damage activation. Despite advancements, gaps remain in modeling

laser-polished components via finite-element methods, particularly in defining the material properties of laser-polished areas where metallurgical transformations occur. Calibrating the damage initiation and fracture loci for the new microstructure is challenging, as is accounting for geometric alterations like pronounced edge rounding induced by laser polishing.
This study aims to address these gaps by conducting multiscale simulations comprising macroscopic simulations of the hole expansion test and microscopic simulations that consider surface roughness. By bridging these scales, the effects of local deformation due to surface roughness and understanding how geometric and metallurgical changes influence the formability of laser-polished DP1000 steel components have been analyzed.

2. Material characterization and laser-polishing

2.1 Material characterization

Table 1 presents the chemical composition of DP1000 steel, a low-alloy steel containing approximately 0.15% carbon. Figure 1 illustrates the fine and homogeneous microstructure of this material. The base microstructure consists of a ferritic matrix with interspersed martensitic islands. These martensitic islands are randomly distributed throughout the ferritic matrix, and martensite bands can be observed.

Table 1: Chemical composition of DP1000 Steel [8].

Element	C	Mg	Si	Cr	Mn
Mass %	0.15	0.01	0.28	0.44	1.883
Element	Ni	P	Mo	S	Cu
Mass %	0.02	0.01	0.113	0.001	0.02

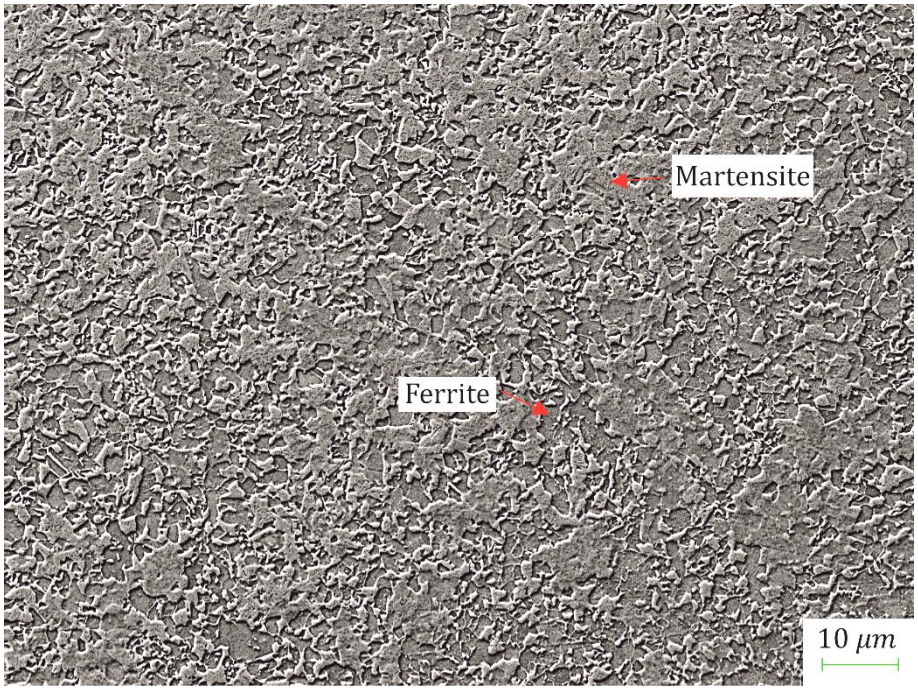

Figure 1: Microstructure of DP1000 Steel in 1000x magnification.

2.2 Laser-polishing on the edge area

Laser-polishing was performed using commercially available equipment, utilizing laser radiation as the energy source to generate a melt pool. Beam-shaping optics were mounted on the machine head, into which the laser beam was coupled via optical fibers. Figure 2a schematically illustrates the optical system used in the experiments. Initially, the laser beam was collimated using a collimating lens, then deflected within the optical system and focused onto the inner edges using a focusing lens, resulting in a circular beam cross-section. The laser beam was positioned such that its dimension on the sheet edge was slightly larger than the edge width. Vertical positioning and precise focusing of the laser beam were achieved by adjusting the collimating lens. A shielding gas device was integrated into the setup to protect the polished area from oxidation. Argon gas flowed through the shielding gas nozzle into the process area, reducing oxidation on the edge surface. In this study, hole expansion samples with an initial sheet thickness of 1.5 mm were pre-manufactured by punching and then finalized with laser polishing.

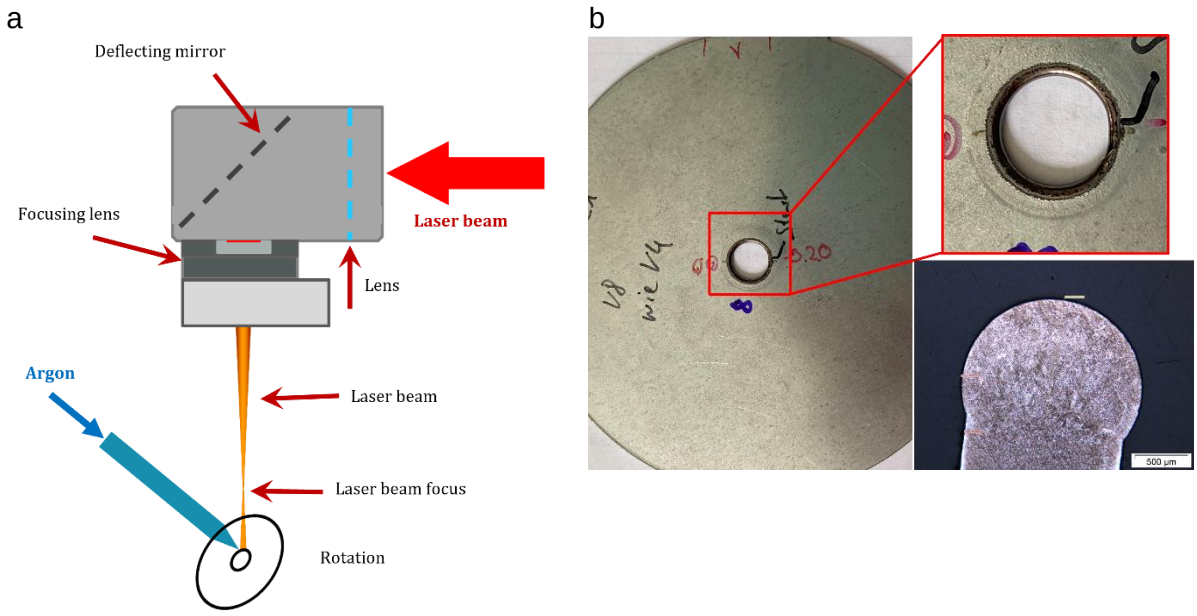

Figure 2: a) Illustration of the laser-polishing process; b) Hole expansion sample with a laser-polished edge.

Figure 2b illustrates the hole expansion sample with a laser-polished edge. Laser polishing was performed using a laser power of 1 kW and a rotation speed of 0.4 m/min. After laser polishing, the edge exhibits a rounded profile accompanied by significant microstructural transformation. Our previous research [8] has demonstrated that laser polishing significantly improves edge roughness and that metallurgical transformations occur in the laser-polished and heat-affected areas. Specifically, in the case of DP1000 steel, the microstructure transforms from a dual-phase to a single-phase martensitic structure. Within this single phase, an increase in grain size and a gradient in grain size distribution have been observed.

3. Material model

Hole expansion tests are influenced by stress state and damage accumulation at the edge, which affect material properties and failure behavior. Since the commonly used von Mises plasticity model does not consider these factors, discrepancies arise between experimental and simulated results. To address this, Bai and Wierzbicki proposed an optimized yield potential that includes the third invariant of the stress deviator J_3, incorporating the Lode angle parameter better to characterize the stress state in the deviatoric plane.

$$\Phi = \sigma_e - \sigma_{yld} \leq 0 \tag{1}$$

$$\sigma_{yld} = \bar{\sigma}\left(\bar{\varepsilon}^{pl}\right)[c_\theta^s + (c_\theta^t - c_\theta^c)(\gamma - \frac{\gamma^{m+1}}{m+1})] \tag{2}$$

c and m are material constants, and $\bar{\sigma}\left(\bar{\varepsilon}^{pl}\right)$ represents the material's flow curve determined from quasi-static uniaxial tensile tests [9]. Bai and Wierzbicki's phenomenological model, applicable to both heavy plates and sheet metals used in this study, is extended by multiplicatively adding terms to the yield stress to account for thermal softening and strain rate hardening, as summarized in Eq.**(3)** [7].

$$\sigma_{yld} = \bar{\sigma}(\bar{\varepsilon}^{pl}) \cdot f(\eta, \bar{\theta}) \cdot f(T) \cdot f(\dot{\varepsilon}) \tag{3}$$

A pure plasticity model is not sufficient to simulate the tests introduced here. For this reason, a coupled damage mechanics model is used, which considers the damage-induced softening phenomena. For this purpose, a damage variable is added to the yield potential introduced in Eq.**(4)**.

$$\Phi = \sigma_e - \sigma_{yld}(1 - D) \leq 0 \tag{4}$$

The $(1 - D)$ term uses the damage variable D and considers damage-induced softening effects. Consequently, damage evolution laws have to be provided. For this purpose, the model applies strain-based and stress-state-dependent criteria that distinguish between damage initiation and fracture. The framework was first described in [18] as a relatively simple uncoupled approach for ductile fracture. Still, continuous development has resulted in a more complex model formulation considering features like non-proportional strain paths or the concurrence between cleavage and ductile fracture mechanisms. Therefore, the most recent model release for ductile fracture [19] is briefly described in the following. By relying on the invariant of the stress tensor I_1 and the deviatoric stress tensor (J_2, J_3), it uses the stress triaxiality η and the Lode angle parameter $\bar{\theta}$ to address the local state of stress.

In the model, it is assumed that under proportional strain paths, damage initiation is triggered when a critical equivalent plastic strain, the so-called “damage initiation strain”, has been reached. Since this critical value depends on the state of stress, it is expressed as the “damage initiation locus” (DIL), providing damage initiation strains $\bar{\varepsilon}^p{}_{ddi}(\eta, \bar{\theta})$ as a function of stress triaxiality and Lode angle parameter:

$$\bar{\varepsilon}^p{}_{ddi}(\eta, \bar{\theta}) = S_k \cdot \left(D_1\ exp\left(-D_2\ \eta\right) - D_3\ exp\left(-D_4\ \eta\right)\right) \cdot \bar{\theta}^2 + D_3\ exp\left(-D_4\ \eta\right) \tag{5}$$

The surface factor S_k is calibrated through multiscale simulations by taking the ratio of damage initiation plastic strains between macroscopic and microscopic models, incorporating artificial surface geometry to account for surface roughness effects. [10].

$$S_k = {\bar{\varepsilon}^p}_{macro} / {\bar{\varepsilon}^p}_{micro} \tag{6}$$

To also allow model predictions for non-proportional strain paths, the model uses an indicator for ductile damage initiation I_{ddi}. It ranges between 0 and 1, with the value of 1 indicating the damage initiation event. I_{ddi} is calculated by integrating the strain history according to the following approach:

$$I_{ddi} = \int_0^{\bar{\varepsilon}^p} \frac{1}{{\bar{\varepsilon}^p}_{ddi}\left(\eta_{average}, \bar{\theta}_{average}\right)} d\bar{\varepsilon}^p \tag{7}$$

The evolution law of damage variable D is described based on the understanding that a material point dissipates a characteristic amount of energy G_f (material constant) between damage initiation and fracture. This is expressed by the following equation:

$$\dot{D} = \frac{\bar{\sigma}_{ddi}}{G_f} \dot{\bar{\varepsilon}}^p \tag{8}$$

Finally, element deletion is applied when the equivalent plastic strain to fracture has been reached. Analogous to damage initiation, it is expressed based on an indicator concept relying on the stress-state dependent "ductile fracture locus" (DFL) given in Eq.**(9)**. The accumulation of ductile fracture indicator, in the case of non-proportional loading, is shown in Eq. **(10)**.

$${\bar{\varepsilon}^p}_{df}(\eta, \bar{\theta}) = S_k \cdot \left(F_1 \ exp\left(-F_2 \ \eta\right) - F_3 \ exp\left(-F_4 \ \eta\right)\right) \cdot \bar{\theta}^2 + F_3 \ exp\left(-F_4 \ \eta\right) \tag{9}$$

$$I_{df} = \int_{{\bar{\varepsilon}^p}_{df}}^{\bar{\varepsilon}^p} \frac{1}{{\bar{\varepsilon}^p}_{df}\left(\eta_{avg}, \bar{\theta}_{avg}\right)} d\bar{\varepsilon}^p \tag{10}$$

All these different indicators are finally merged into the following damage evolution law in Eq. **(11)**:

$$D = \begin{cases} 0, & \bar{\varepsilon}^p \leq {\bar{\varepsilon}^p}_{ddi} \\ \frac{\bar{\sigma}_{ddi}}{G_f}\left({\bar{\varepsilon}^p}_{df} - {\bar{\varepsilon}^p}_{ddi}\right) \cdot \int_{{\bar{\varepsilon}^p}_{ddi}}^{{\bar{\varepsilon}^p}_{df}} d\bar{\varepsilon}^p, & {\bar{\varepsilon}^p}_{ddi} < \bar{\varepsilon}^p < {\bar{\varepsilon}^p}_{df} \\ 1, & {\bar{\varepsilon}^p}_{df} < \bar{\varepsilon}^p \end{cases} \tag{11}$$

4. Microstructure characterization and surface characterization

4.1 Microstructure characterization

The microstructure of different regions within the laser-polished area was analyzed using scanning electron microscopy (SEM). The laser-polishing process induced a phase

transformation, forming a pure acicular martensite structure that replaced the original dual-phase microstructure. Additionally, the transition zone exhibited a mixed microstructure consisting of acicular and island structures, collectively forming the martensite phase's morphology. Electron Backscatter Diffraction (EBSD) analysis was conducted to investigate the sample's grain size and texture distribution. The findings revealed a distinct grain size gradient from the center of the laser-polished zone to the transition zone. Notably, the number fraction of grains with a diameter of 6 μm observed in the sample was twice that of the original material. These results indicate that the laser-polishing process significantly impacts the microstructural characteristics of the sample.

Various notched specimens—including centrally notched (round and elliptical), dog-bone, and plane-strain samples with varying notch sizes—were tensile tested under quasi-static conditions to identify the damage parameter across a wide range of stress triaxiality and Lode angle parameters (Table 2).

Table 2: Calibrated material parameters for martensitic steel.

Parameter	a	A	n	b	q	p	w	E
Value	0.95	280MPa	0.077	878	249.8MPa	253	-119.4	202.3GPa
Parameter	m	c_θ^s	c_θ^t	c_θ^c	D_1	D_2	D_3	D_4
Value	6	0.98	1	0	1.375	2.2	0.388	1.72
Parameter	ν	F_1	F_2	F_3	F_4	G_f	S_k	
Value	0.3	1.72	1.25	0.7	1.125	$3600\,\frac{J}{mm^3}$	0.702	

4.2 Surface characterization

This study employed a NanoFocus μsoft white-light confocal microscope to analyze the edge surface topography of hole expansion samples. This technology captures detailed surface structures by transmitting light through pinholes and lenses at various focal distances, with reflected light collected on a camera sensor [11]. The microscope was configured with a 20× objective lens and a shutter speed of 1/100 s, providing high-resolution measurements of 1.6 μm in-plane (X and Y directions) and 5 nm out-of-plane over an area of 1.5 mm × 1.5 mm.

A previous study [8] comprehensively analyzed punching and laser polishing samples' 2D and 3D surface roughness. The results demonstrated that laser polishing yields a more uniform and refined surface, with improved characteristics such as maximum height and arithmetic mean height. These findings indicate that laser polishing is superior to punching in achieving smoother and more homogeneous surface profiles.

Surface measurement data from confocal microscopy were analyzed as spatial signals defined by variations in the X and Y directions. To enhance analysis, we applied the Fourier transformation to convert spatial domain signals into the frequency domain, leveraging the sinusoidal nature of real-world signals. This approach allows detailed signal modification using mathematical tools available in the frequency domain. Fourier transformation (Eq.**(12)**) decomposes signals into sinusoids with varying frequencies, while the inverse Fourier transformation (Eq.**(13)**) reconstructs processed signals back into the spatial domain.

$$F(\lambda_x, \lambda_y) = \sum_{x=0}^{X-1} \sum_{y=0}^{Y-1} f(x,y) * e^{-2\pi i * (\frac{x}{X\lambda_x} + \frac{y}{Y\lambda_y})} \quad (12)$$

$$f(x,y) = \frac{1}{XY} \sum_{\lambda_x=0}^{X-1} \sum_{\lambda_y=0}^{Y-1} F(t,k) * e^{-2\pi i * (\frac{x}{X\lambda_x} + \frac{y}{Y\lambda_y})} \quad (13)$$

To isolate waviness and roughness components, we utilized Gaussian filters in the frequency domain. Low-pass filters $L(\lambda_x, \lambda_y)$ permit low-frequency components while attenuating high frequencies, defined by cutoff wavelengths λ_{xc} and λ_{yc}. High-pass filters are defined as $H(\lambda_x, \lambda_y)$. Cutoff values of $\lambda_c = 385\mu$m for high-pass and $\lambda_s = 1\mu$m for low-pass filters based on microscope measurements and simulation requirements has been selected.

$$L(\lambda_x, \lambda_y) = e^{-\pi\beta\left[(\frac{\lambda_{xc}}{\lambda_x})^2 + (\frac{\lambda_{yc}}{\lambda_y})^2\right]}, H(\lambda_x, \lambda_y) = 1 - L(\lambda_x, \lambda_y) \quad (14)$$

After filtering, the data is reconstructed into an artificial surface with predefined resolutions for export to ABAQUS CAE. Incorporating macroscopic simulation data as boundary conditions, the submodel's free edge is replaced with new geometry, integrating surface roughness into the simulation.

5. Results and discussion

Hole expansion tests with laser-polished edge geometries were simulated using a multiscale modeling approach. Macroscopic simulations were first conducted without explicit surface roughness, focusing solely on the geometrical changes introduced by laser polishing. Subsequently, microscopic simulations incorporated measured surface roughness to evaluate its influence on damage initiation.

Figure 3 presents the spatial distribution of the damage initiation indicator I_{ddi} in both macroscopic and microscopic models. This indicator ranges from 0 to 1, with $I_{ddi} = 1$ marking the onset of local damage. Due to the modified edge geometry resulting from laser-polishing, the critical damage zone shifts from the lower to the upper edge region, driven by altered local stress states.

In the macroscopic simulation, the first element reaching $I_{ddi} = 1$ defines the critical element. A corresponding microscopic submodel is then positioned at this location using ABAQUS submodeling. The boundary conditions for the submodel are directly extracted from the macroscopic simulation to ensure mechanical consistency. The measured surface roughness profile is applied in the microscopic model to reflect the actual edge topography.

To reduce variability, the macroscopic model assumes an idealized, smooth laser-polished surface. Figure 3 corresponds to the loading condition at the increment where the first element in the macroscopic model reaches $I_{ddi} = 1$. This is defined as the macroscopic critical increment, denoted as t_{macro}.

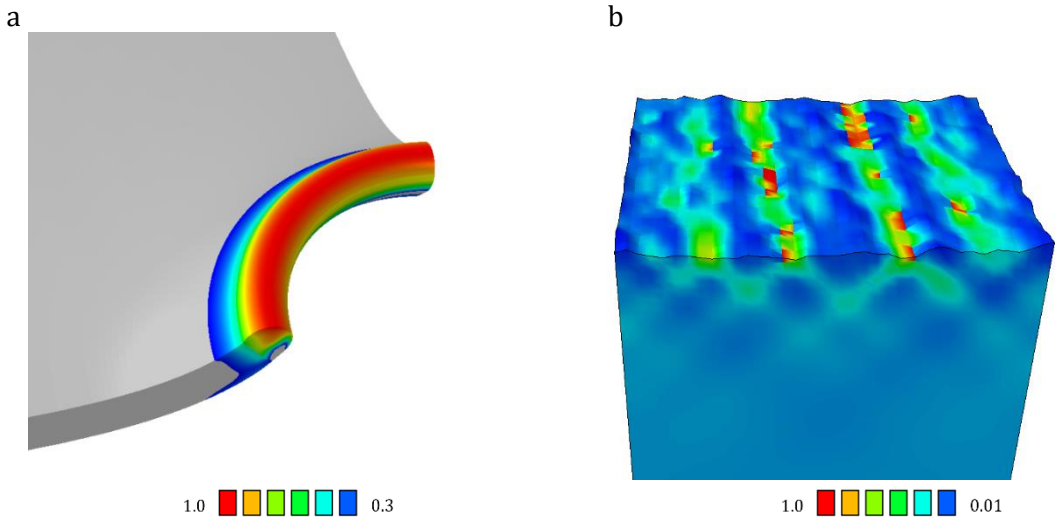

Figure 3: Damage initiation indicator in a) macroscopic simulation and b) microscopic simulation.

In the microscopic simulation, the critical element reaches $I_{ddi} = 1$ at a later increment, denoted t_{micro}, due to local strain accommodation caused by surface roughness. The actual increment at which damage initiates in the microscopic model is noted as t_{new}, and this corrected damage onset is used to refine the damage model. These increments are visualized and correlated through strain path analysis in Figure 4.

To incorporate the local effects of surface roughness into the macroscopic model, a surface correction factor s_k is introduced (Eq. (6)). This factor adjusts both the damage initiation threshold and the ductile fracture locus. For the laser-polished profile, the calibrated value is $s_k = 0.702$, which reflects the detrimental impact of micro-roughness features.

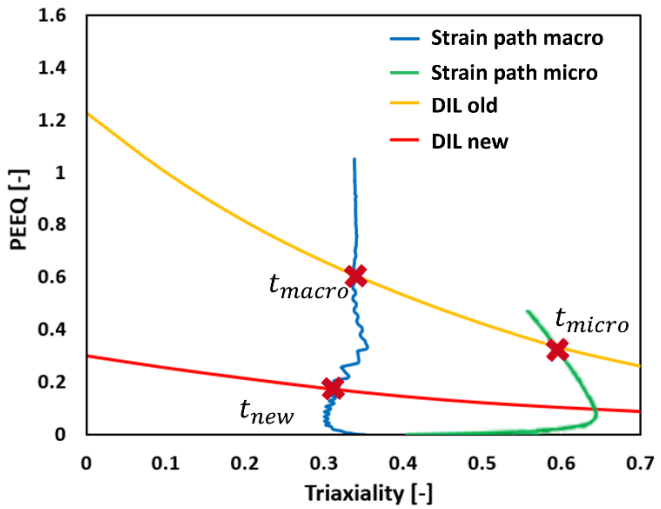

Figure 4: Strain path of the critical element in macroscopic simulation and microscopic model.

Figure 5a compares experimental and simulated force-displacement curves under identical hole expansion loading conditions. Results are shown for three cases: simulations without s_k, simulations with the calibrated s_k, and experimental results. The simulations without surface

correction consistently overpredict the force response. In contrast, incorporating $s_k = 0.702$ yields a close match to experimental results, though slightly conservative.
Figure 5b shows the hole expansion ratio from both simulations and experiments. The simulation incorporating surface effects via s_k matches the experimental HER values well, validating the proposed multiscale modeling framework.

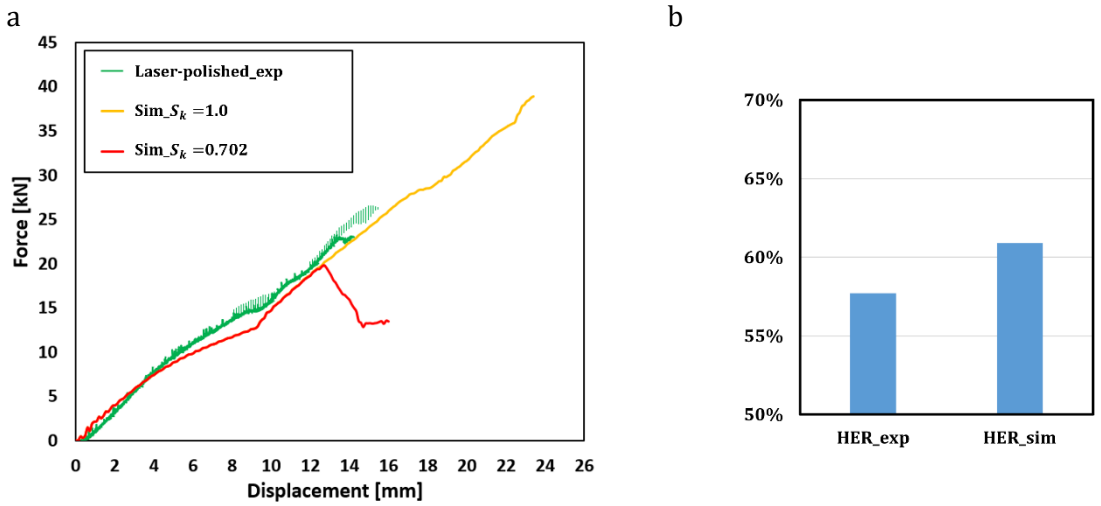

Figure 5: a) Force-Displacement curves and b) HER.

6. Conclusion

The fully calibrated MBW material model, incorporating the surface factor S_k, effectively simulates the edge geometries in the hole expansion tests, yielding force-displacement responses closely aligned with experimental results. By integrating S_k into the MBW model, the simulations achieve higher accuracy in predicting force-displacement behavior than conventional models that neglect surface roughness effects.

References

[1] Kohei Hasegawa, Kenji Kawamura, Toshiaki Urabe, and Yoshihiro Hosoya, "Effects of Microstructure on Stretch-flange-formability of 980 MPa Grade Cold-rolled Ultra High Strength Steel Sheets," *ISIJ International*, vol. 44, no. 3, pp. 603–609, 2004, doi: 10.2355/isijinternational.44.603.

[2] N. H. Abid, R. K. Abu Al-Rub, and A. N. Palazotto, "Micromechanical finite element analysis of the effects of martensite morphology on the overall mechanical behavior of dual phase steel," *International Journal of Solids and Structures*, 104-105, pp. 8–24, 2017, doi: 10.1016/j.ijsolstr.2016.11.005.

[3] Nikhare, "Analysis of hole expansion limit through biaxial test," *Materials Today: Proceedings*, vol. 5, 1, Part 1, pp. 44–50, 2018, doi: 10.1016/j.matpr.2017.11.051.

[4] V. Balisetty, U. Chakkingal, and S. Venugopal, "Evaluation of stretch flangeability of dual-phase steels by hole expansion test," *Int J Adv Manuf Technol*, vol. 114, 1-2, pp. 205–217, 2021, doi: 10.1007/s00170-021-06850-9.

[5] E. V. Bordatchev, A. M. K. Hafiz, and O. R. Tutunea-Fatan, "Performance of laser polishing in finishing of metallic surfaces," *Int J Adv Manuf Technol*, vol. 73, 1-4, pp. 35–52, 2014, doi: 10.1007/s00170-014-5761-3.

[6] Y. Bai and T. Wierzbicki, "A new model of metal plasticity and fracture with pressure and Lode dependence," *International Journal of Plasticity*, vol. 24, no. 6, pp. 1071–1096, 2008, doi: 10.1016/j.ijplas.2007.09.004.

[7] J. Lian, M. Sharaf, F. Archie, and S. Münstermann, "A hybrid approach for modelling of plasticity and failure behaviour of advanced high-strength steel sheets," *International Journal of Damage Mechanics*, vol. 22, no. 2, pp. 188–218, 2013, doi: 10.1177/1056789512439319.

[8] D. Li *et al.,* "Optimizing sheet metal edge quality with laser-polishing: surface characterization and performance evaluation," *Int J Mater Form*, vol. 17, no. 5, 2024, doi: 10.1007/s12289-024-01847-7.

[9] B. Wu, N. Vajragupta, J. Lian, U. Hangen, P. Wechsuwanmanee, and S. Münstermann, "Prediction of plasticity and damage initiation behaviour of C45E + N steel by micromechanical modelling," *Materials & Design*, vol. 121, pp. 154–166, 2017, doi: 10.1016/j.matdes.2017.02.032.

[10] P. Wechsuwanmanee, J. Lian, W. Liu, and S. Münstermann, "Numerical Evaluation of Surface Roughness Influences on Cold Formability of Dual-Phase Steel," *steel research int.*, vol. 91, no. 11, 2020, doi: 10.1002/srin.202000141.

[11] B. Rosa, J.-Y. Hascoët, and P. Mognol, "Topography modeling of laser polishing on AISI 316L milled surfaces," *Mechanics & Industry*, vol. 15, no. 1, pp. 51–61, 2014, doi: 10.1051/meca/2014003.